

Received 17 August 2024, accepted 5 September 2024, date of publication 10 September 2024, date of current version 20 September 2024.

Digital Object Identifier 10.1109/ACCESS.2024.3456818



Fault Detection and Isolation in Wind Turbines: Type-3 Fuzzy Logic Systems and Adaptive Random Search Learning

AIMEI ZHOU¹, ZHIPING ZHU², EBRAHIM GHADERPOUR[®]³, ALI DOKHT SHAKIBJOO[®]⁴, HAMID TAGHAVIFAR[®]⁵, (Senior Member, IEEE), ARDASHIR MOHAMMADZADEH[®]⁶, AND CHUNWEI ZHANG[®]⁷

Corresponding authors: Ebrahim Ghaderpour (ebrahim.ghaderpour@uniroma1.it), Ardashir Mohammadzadeh (a.mzadeh@sut.edu.cn), Chunwei Zhang (zhangchunwei@sut.edu.cn), and Zhiping Zhu (130@linix.com.cn)

This work was supported in part by the Sapienza University of Rome.

ABSTRACT Ensuring the reliability of wind energy conversion systems (WECSs) is a crucial task for maximizing energy capture from the wind. A detailed model incorporating mechanical and electrical components is essential for accurately diagnosing system errors and assessing their impact on subsystems. Additionally, a fault detection and isolation system is necessary to quickly identify recurring faults and prevent significant economic losses. This study introduces a fault detection and isolation system using dynamic model of WECS based on type-3 (T3) fuzzy logic systems (FLSs). The adaptive random search (ARS) is employed to optimize the T3-FLS parameters and structure for enhanced fault detection accuracy. T3-FLSs handle higher levels of uncertainty and variability compared to traditional FLSs and neural networks. This allows for more accurate fault detection in complex and dynamic systems. One T3-FLS model replicates the system's normal operation, while another simulates faulty conditions. These T3-FLS models are run in parallel with the actual plant, allowing for comparison of their outputs with the real system's outputs to pinpoint error timing and location. The ARS is utilized to train the T3-FLSs, eliminating the need for gradient expression calculations. The appropriate number of rules for the T3-FLS is determined using Akaike and final prediction error criteria. Simulation results demonstrate the system's ability to rapidly detect and isolate errors with minimal false alarms. This research framework can be applied to identify errors in various system components effectively.

INDEX TERMS Fault detection, wind energy, isolation, type-3 fuzzy logic, control systems, machine learning.

I. INTRODUCTION

Energy distribution network and transportation systems have become a key element in daily life nowadays. Therefore, an error in any of their components will disrupt the

The associate editor coordinating the review of this manuscript and approving it for publication was Qi Zhou.

performance of the entire system. Generally, an error is defined as changes in the system's behavior, such that the system is no longer able to fulfill its goals and tasks. Reliability for any plan is one of its very important features, guaranteed by eliminating the weaknesses and errors that occurred in the past. One of the methods of achieving reliability is the development of monitoring systems and

¹School of Intelligent Manufacturing, Zhejiang Guangsha Vocational and Technical University of Construction, Dongyang 322100, China

²Zhejiang LINIX Motor Company Ltd., Dongyang 322100, China

³Department of Earth Sciences, CERI Research Centre, Sapienza University of Rome, 00185 Rome, Italy

⁴Department of Electrical Engineering, Ahrar Institute of Technology and Higher Education, Rasht 41931-63591, Iran

⁵Department of Mechanical, Industrial and Aerospace Engineering, Concordia University, Montreal, QC H3G 1M8, Canada

⁶Department of Computational and Data Science, Astana IT University, 020000 Astana, Kazakhstan

⁷Multidisciplinary Center for Infrastructure Engineering, Shenyang University of Technology, Shenyang Economic-Technological Area, Shenyang, Liaoning 110870, China



fault diagnosis and isolation (FDIS) systems. Error detection for industrial problems has become very important recently. In these systems, economic issues and user euphoria are important [1], [2], [3].

Many faults can be detected in a wind energy conversion system (WECS) while the faulty component continues to operate [4]. Therefore, the repair operation can be done at the appointed time. The absence of urgency is crucial for offshore power plants, as adverse conditions like typhoons can result in repair operations being delayed for weeks. With FDIS, a system can often be repaired before a faulty component causes damage. These cases are also very important in WECSs. Although the implementation of FDIS requires investment at the beginning, the continuous production of energy without any outages will return the primary investment cost. Because of their remote location, wind farms benefit more from the benefits of such a system, because very high costs must be paid for transportation to these places. Countries with weak transportation systems to reach the wind farms and turbines should use FDIS to avoid energy cutting and good maintenance costs [5], [6], [7].

Since replacing the basic components of a WECS is hard and expensive, developed maintenance solutions can reduce costs. Therefore, an FDIS for WECS has advantages, such as preventing premature failure, reducing maintenance costs, monitoring remote sites, improving the capacity factor, and supporting the further development of WECS [8]. Generally, error diagnosis methods are divided into two cases: error detection based on hardware redundancy and error detection based on analytical redundancy. On the other hand, the redundancy method can be classified into methods based on the quantitative model and methods based on the qualitative model. Quantitative model-based approaches use mathematical dynamics and control theory to produce residuals in the fault detection system, while qualitative models use intelligent methods to obtain differences between real and predicted behaviors [9].

Diagnosing and isolating the errors that occur continuously in WECS has also attracted attention, recently. For example, in [10], by the use of a linear model of the mechanical components of a case-study WECS, a fault-tolerant system is suggested. In [11], wind turbine fault detection has been done for the linear dynamics of mechanical components, and only one fault has been investigated. In [12], the occurrence of an error in the induction generator has been considered. In [10], continuous errors in the wind turbine have been identified using supervisory control and data acquisition. In [13], bearing errors have been detected using the data mining method. In [14], using practical information from the conditions monitoring system, the errors related to the wind turbine brake system have been identified.

In recent years, extensive research has been done in the field of techniques using quantitative models [15] and qualitative models [16]. In general, these techniques are classified as system identification methods, observer-based methods, signal analysis methods, artificial intelligence methods, and expert systems. Recently, neural networks (NNs) have been intensively studied and successfully used in dynamic systems [17]. The primary idea behind using NNs for fault detection involves their ability to learn complex patterns and relationships within large data sets. NNs can analyze historical data from machinery to predict potential failures before they occur, allowing for timely maintenance. By training on normal operating conditions, NNs can identify deviations in system behavior that may indicate faults. Local recurrent NNs offer the advantage of having a structure that closely resembles that of a static NN. In these networks, dynamic neurons replace static neurons. One type of dynamic neuron generates dynamics by utilizing a filter within the neuron dynamics. As a result, this NN does not incorporate global feedback. These types of feedback make network design and training difficult. The design of these NNs is between the design of forward and backward NNs. This class of neural networks is called global feedforward-local backward NNs [18]. Recurrent NNs with infinite impulse response (IIR) filters have been successfully used for modeling, error detection, and forecasting of time series [19]. In [18], applications for fault detection by these NNs are presented in the splitting system of the fluid actuator and the direct current (DC) motor. In [20], a recurrent NN is presented by combining a neuron structure with an IIR filter, and by using the designed NN, a fault detection model is suggested.

Fuzzy systems are also applied in fault detection systems to handle uncertainties and imprecise data that are common in real-world scenarios. FLSs can be used to define rules for fault detection based on expert knowledge or historical data. These rules can capture the complex relationships between input variables and fault conditions, allowing the system to make accurate decisions even in the presence of uncertainty. For example, the research [21] focuses on designing an FLS-based controller for active/reactive power during transients and faults. The study includes four different models, analyzing their performance under various fault conditions. In [22] a hybrid method is suggested by combining machine learning with zonotopic observers. It begins by identifying a wind turbine's dynamic model using an adaptive network-based FLS. However, recently advanced FLSs with higher flexibility and estimation capability have been introduced, that can be used for this problem. In [23] the fault detection in hydrodynamic mechanical seals is studied and a convolutional network is

Type-2 (T2) and type-3 (T3) FLSs offer a flexible and effective approach to fault detection by handling uncertainties and imprecisions in data, making them well-suited for applications in diverse industries, such as manufacturing, automotive, and aerospace [24], [25], [26]. However, T3-FLS based fault detection for wind turbines has not been studied. T2-FLSs based systems have been studied in some studies. For example, in [27], a multiple first-order dynamic fractional-order T2-FLSs is proposed to model and control



load frequency in power systems. In [28], an interval T2-FLS is suggested for analyzing the stability of a generator-based wind turbine system in the presence of external disturbances. The controller aims to reduce uncertainties. The study utilizes fuzzy modeling techniques and constructs a Lyapunov functional to design a nonfragile sampled-data controller. In [29], a hybrid method is introduced that uses a multi-objective evolutionary algorithm to maintain key components and optimize maintenance plans in offshore substations for renewable energy applications. The method addresses operational changes and uncertainties through system optimization based on FLSs and hidden Markov model technology. Results show that this approach can effectively handle uncertainties in condition-based maintenance for renewable energy applications. The study [30] focuses on creating a decision-making system that considers environmental factors to evaluate Ireland's offshore wind sites for sustainable development. The model integrates interval T2-FLSs and advanced energy economic metrics to make more precise decisions.

In [31], a hybrid model is suggested to improve the precision of a support vector machine (SVM) classifier for detecting stator winding short circuit faults in induction motors. The model involves extracting statistical features from healthy and defective data sets, reducing dimensions using principal component analysis, constructing SVMs based on training data, optimizing SVM parameters with a chaotic particle swarm optimization algorithm, and combining SVMs with T2-FLSs. The model is tested on measured stator current data from a three-phase induction motor, achieving an average accuracy of 98.4% in detecting stator winding faults under various load conditions. In [32], a shadowed T2-FLS is developed with m cuckoo search and flower pollination for dynamic parameter adaptation. The designed system is shown to outperform type-1 FLSs. In [33], a T2-FLS based wind speed prediction model is designed that focuses on selecting important input variables to reduce complexity. The model utilizes fuzzy curves and Gaussian membership functions to improve prediction accuracy, with the recursive least squares method used for parameter identification. The suggested model aims to achieve deterministic wind speed prediction with high robustness.

Type-3 FLSs are an extension of traditional FLSs that allow for more complex and flexible modeling of uncertainty and imprecision [34]. In T3-FLSs, the membership functions can take on a wider range of shapes and can be non-standard, allowing for a more nuanced representation of uncertainty. This makes T3-FLSs well-suited for applications where uncertainty is high or where traditional FLSs may not provide enough flexibility. In various applications, the superiority of T3-FLSs have been shown, such as control of surface vehicles [35], modeling problems [36], monitoring systems [37], control systems [38], [39], forecasting problems [40], optimization problems [41], and many others. The literature review shows that

- Modeling of WECSs has not been studied entirely, and in many existing methods, a linear model has been employed to construct a fault detection system.
- In many methods, the fault detection discussion has been taken into consideration, and the isolation errors have been ignored.
- In few studies, FLS-based methods have been proposed, however, conventional FLSs have limited flexibility in capturing complex relationships between input variables, which can hinder their ability to accurately detect faults in dynamic and uncertain environments.
- Most of the existing models are sensitive to noise and disturbances in the input data, leading to false alarms or missed detections in fault detection applications.

Regarding the discussion above, in the present research, using the T3-FLS based full nonlinear model of the wind power conversion system including electrical and mechanical parts, a fault diagnosis/isolation system is designed, which can diagnose and isolate the errors of angular speed sensor and the pitch actuator. Using a nonlinear-based model will lead to better results closer to the real uncertain situation. T3-FLSs can handle uncertainties more effectively compared to type-1 and type-2 FLSs, resulting in more accurate fault detection. The adaptive random search method (ARS) is used to train the T3-FLS model to enhance the accuracy and construct an adaptive fault detection system. The main contributions of the present study are as follows.

- A new fault detection and isolation system is introduced using a dynamic model of WECS based on T3-FLSs.
- A new ARS is employed to optimize the T3-FLS parameters and structure for enhanced fault detection accuracy, eliminating the need for gradient expression calculations.
- The appropriate number of rules for the T3-FLS is determined using Akaike and final prediction error criteria.
- The developed T3-FLS can handle higher levels of uncertainty and allow for more accurate fault detection.
- The suggested system is capable of detecting the error timing and location and can rapidly detect and isolate errors with minimal false alarms.

II. WIND ENERGY CONVERSION SYSTEM

The common part between all presented models is dividing WECS into subsystems and deriving the mathematical dynamics. The model used in this research is shown in Fig. 1. In this figure, the turbine angle adjustment mechanism is omitted. Because the tower is in oscillation, $v_r(t)$ is obtained from the difference between the speed of the chassis, $\dot{\chi}_t(t)$, and the wind speed.

Additionally, the rotor aerodynamic torque denoted as $T_r(t)$, is transmitted to the generator via the drive components, which consist of high-speed and low-speed axes as well as the gearbox. The induction generator transforms mechanical power into electrical energy and is linked to



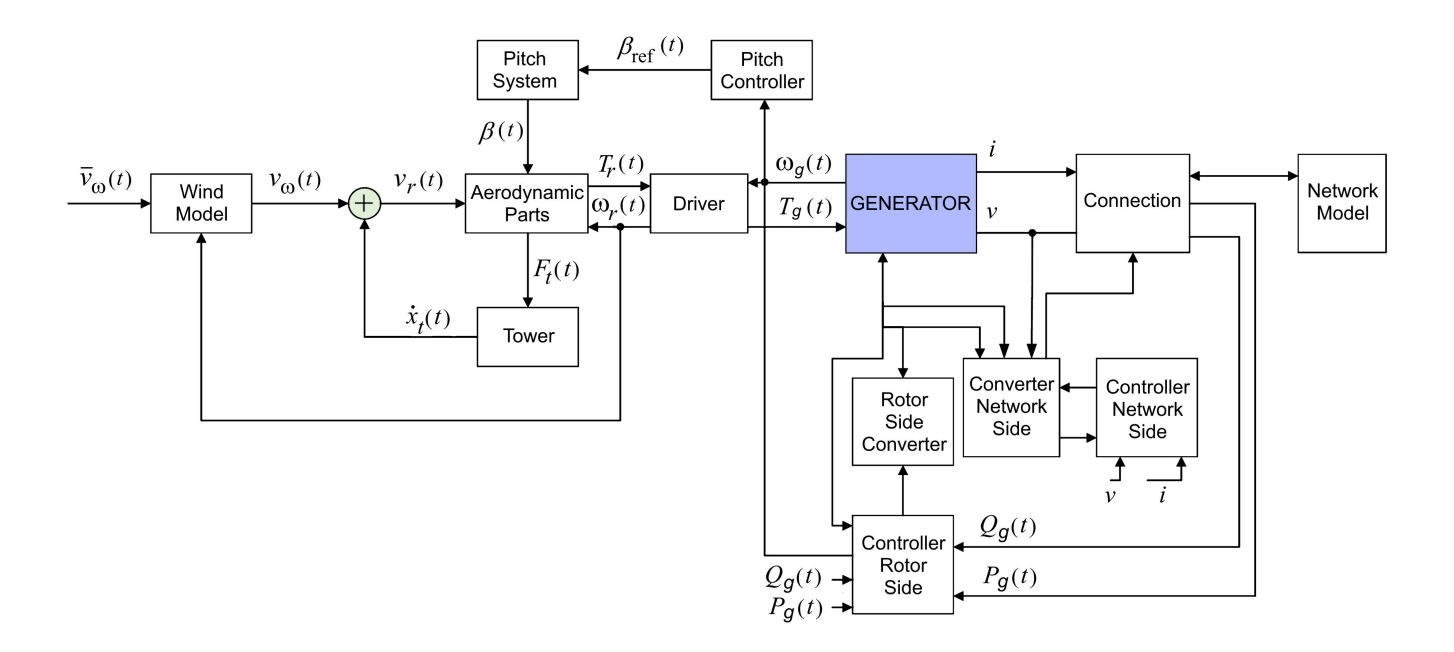


FIGURE 1. Modeling diagram of WECS.

the energy grid. An interface is utilized to determine the active/reactive power. The network model also encompasses the local load, transformer, and an infinite bus. Furthermore, converters, rotor side converter controllers (RSC), and grid side converter (GSC) are included in this model.

At first, the equations of the mechanical parts of WECS are examined [42].

$$V_{\omega}(t) = \bar{V}_{\omega}(t) + v_{ws}(t) + v_{ts}(t) + v_{tu}(t) \tag{1}$$

In Equation (1), $V_{\omega}(t)$ is the wind speed which includes the effect of the tower, the vortex airflow, and the sudden deviation of the wind path, $\bar{V}_{\omega}(t)$ is the average wind speed, $v_{ws}(t)$ is the effect of the sudden deviation of the wind path, $v_{ts}(t)$ is the element indicating the effect of the tower, and $v_{tu}(t)$ is the effect of the vortex airflow. Also, Equation (2) is employed to model the aerodynamic parts, in which $P_r(t)$ is the energy received by the turbine rotor, $\beta(t)$ denotes the pitch angle, $\lambda(t)$ represents the speed of the blade tip, $C_p(\lambda(t), \beta(t))$ show the energy factor of the turbine, A is the surface of the rotor in square meters, v_r is the effective wind speed on the rotor in meters per second, ρ denotes the air density in kg/m³ and $T_r(t)$ rotor aerodynamic torque.

$$P_r(t) = \frac{1}{2} C_p(\lambda(t), \beta(t)) \rho A v_r^3(t)$$

$$T_r(t) = \frac{P_r(t)}{\omega_r(t)} = \frac{C_p(\lambda(t), \beta(t))}{\omega_r(t)} 0.5 \rho A v_r^3(t)$$
(2)

where $C_t(\lambda(t), \beta(t))$ denotes thrust coefficient. The force function is given by Equation (3).

$$F_t(t) = 0.5\rho A v_r^2(t) C_t \left(\lambda(t), \beta(t) \right) \tag{3}$$

The aerodynamic torque is converted by the drive parts into the torque applied to the generator. The gear wheel converts the rotational speed to the generator speed with a factor called the gear ratio. Equations (4)-(6) are used to model the drive parts, including the low-speed axis, the gear, and the highspeed axis.

$$J_r \dot{\omega}_r = T_r - K_{dt} \theta_{\delta} B_{dt} \dot{\theta}_{\delta} \tag{4}$$

$$J_g N_g \dot{\omega}_g = -T_g N_g + K_{dt} \theta_\delta B_{dt} \dot{\theta}_\delta \tag{5}$$

$$\dot{\theta}_{\delta} = \omega_r - \omega_\varrho / N_\varrho \tag{6}$$

In Equations (4)-(6), the rotor inertia and low-speed axis is shown by J_r . T_r denotes the torque in low-speed axis and ω_r denotes the rotor speed. Note that J_r acts in the same direction as ω_r . Also, it is a massless viscous damping rotational spring, with a spring stiffness coefficient of K_{dt} and a damping coefficient of B_{dt} . The gear ratio is shown by N_g and the inertia of the gear, high-speed axis, and generator is shown by J_g . In these equations, T_g and ω_g represent the generator torque and rotor rotational speed, respectively. Note that T_g acts against the direction of rotation. Also, the negative values in the two curves above are set to zero. The thrust force causes the tower to move forward and backward by fluctuating tower with a mass-spring-damper system based on Equation (7) is modeled. In this regard, $F_{th}(t)$ denotes the operating force, and at the height of the vane ball, B_t is coefficient damping, K_t the twist coefficient of the tower, M_t is the mass of the top of the tower and $\chi_t(t)$ represents the displacement of the chassis. Tower oscillation impact on the wind speed seen from rotor. The wind speed is modeled based on Equation (8).

$$M_t \dot{\chi}_t(t) = F_{th}(t) - B_t \dot{\chi}_t(t) - K_t \chi_t(t)$$
 (7)

$$v_r(t) = V_{\omega}(t) - \dot{\chi}_t(t) \tag{8}$$

Pitch driver is modeled by Equation (9), where in this equation, $\beta(t)$ and $\beta_{ref}(t)$ denote the angle reference pitch

IEEE Access

angle, ω_n and ν represent the natural frequency and damping ratio. Equation (9) explains the action of the superimposed stimulus when this stimulus applies within certain limits. The upper and lower limits should be considered for $\beta(t)$ and $\dot{\beta}(t)$ (the physical limits of the drive). These limits were considered in the form of Table 1 [43].

$$\ddot{\beta}(t) = -2vw_n\dot{\beta}(t) - \omega_n^2\beta(t) - \omega_n^2\beta_{\text{ref}}(t)$$
 (9)

TABLE 1. Limitations of pitch.

Lower limit	Upper limit	Parameter
-5°	90°	$\beta(t)$
$-10^{\circ}/s$	$10^{\circ}/s$	$\gamma \beta(t)/dt$

The equations of modeling of the electrical parts of WECS are also as follows.

$$V_{qs} = R_s i_{qs} + \frac{\gamma}{dt} \varphi_{qs} + \omega_s \varphi_{ds}$$
 (10)

$$V_{ds} = R_s i_{ds} + \frac{\gamma}{dt} \varphi_{ds} + \omega_s \varphi_{qs}$$
 (11)

$$V_{qr} = i_{qr}R_r + \frac{\gamma}{dt}\varphi_{qr} + \varphi_{dr}(\omega_s - \omega_r)$$
 (12)

$$V_{dr} = i_{dr}R_r + \frac{\gamma}{dt}\varphi_{dr} + \varphi_{qr}(\omega_s - \omega_r)$$
 (13)

Equations (10)-(13) display the voltage equations of the stator/rotor in reference frame. All parameters in this model are related to the stator, R_s/R_r is the resistances of the stator/rotor, ω_s denotes the angular speed, ω_r is the rotor angular speed, φ_{qs} and φ_{qs} are the stator flux in the direction of d and q axis, and also φ_{qr} and φ_{qr} of the rotor flux are in the direction of d and q axis. Also, stator and rotor flux are shown in Equations (14)-(17). The equations $L_r = L_{lr} + L_m/L_s = L_{ls} + L_m$ is the inductance of the stator/rotor.

$$\varphi_{as} = L_s i_{as} + L_m i_{ar} \tag{14}$$

$$\varphi_{ds} = L_s i_{ds} + L_m i_{dr} \tag{15}$$

$$\varphi_{qr} = L_r i_{qr} + L_m i_{qs} \tag{16}$$

$$\varphi_{dr} = L_r i_{dr} + L_m i_{ds} \tag{17}$$

Electromagnetic torque is written as Equation (18), in which, p is the pole numbers of the machine. Two equations related to the mechanical parts of the machine are also shown in Equations (19) and (20), in which H is the inertia constant of the load and rotor, F is the coefficient of friction of the viscosity of the load and rotor, T_g and ω_g denote the mechanical torque and angular velocity. θ_g is the rotor angular position.

$$T_e = 1.5p \left(\varphi_{ds} i_{qs} - \varphi_{qs} i_{ds} \right) \tag{18}$$

$$\frac{\gamma}{dt}\omega_g = \frac{1}{2H}\left(T_e - Fw_g - T_g\right) \tag{19}$$

$$\frac{\gamma}{dt}\theta_g = \omega_g \tag{20}$$

The grid side converter and DC link capacitor are modeled using Equations (21)-(24). R_g/L_g represents the resistance/inductance, C is the link capacitor capacity, V_{dc} is the

capacitor voltage, P_r/P_g is the active/reactive power.

$$V_{dg} = R_g i_{dg} + L_g \frac{\gamma}{dt} i_{dg} - \omega_s L_g i_{qg} + V_{ds}$$
 (21)

$$V_{qg} = R_g i_{qg} + L_g \frac{\widetilde{\gamma}}{dt} i_{qg} - \omega_s L_g i_{qg} + V_{qs}$$
 (22)

$$P_g = \frac{3}{2} \left(V_{ds} I_{dg} + V_{qs} I_{qg} \right) \tag{23}$$

$$\frac{dV_{dc}}{dt} = \frac{P}{V_{dc}C} = \frac{P_r - P_g}{V_{dc}C} = \frac{P_e - P_s - P_g}{V_{dc}C}$$
(24)

The WECS has three types of control systems: RSC, GSC, and pitch control systems. The following equations are used to control RSC.

$$V_{dr}^* = \sigma L_r V_{dr}' + R_r i_{dr} - s w_s \sigma L_r i_{qr} - s w_s \left(\frac{L_m}{L_s}\right) \varphi_{qs}$$

$$V_{qr}^* = \sigma L_r V_{qr}' + R_r i_{qr} - s w_s \sigma L_r i_{dr} - s w_s \left(\frac{L_m}{L_s}\right) \varphi_{ds}$$

In the equations above, the control voltages V_{dr}^* and V_{qr}^* are obtained using proportional and integral (PI) controllers and by comparing the obtained currents i_{dr} and i_{qr} with the reference values i_{dr}^* and i_{qr}^* according to the following equation.

$$V'_{dr} = \frac{di_{dr}}{dt} = K_{p1} (i_{dr}^* - i_{dr}) + K_{I1} \int (i_{dr}^* - i_{dr}) dt$$

$$V'_{qr} = \frac{di_{qr}}{dt} = K_{p1} (i_{qr}^* - i_{qr}) + K_{I1} \int (i_{qr}^* - i_{qr}) dt$$

In the equations above, K_{p1} denotes the proportional coefficient and K_{I1} is the integral coefficient controlling PI. For GSC control, Equations (25) and (26) are considered [44].

$$V_{dg}^* = R_g \dot{i}_{dg} + L_g \dot{V}_{dg} - \omega_s \sigma L_g i_{gg} + V_{ds}$$
 (25)

$$V_{qg}^* = R_g \acute{i}_{qg} + L_g \acute{V}_{qg} + \omega_s \sigma L_g i_{dg} + V_{qs}$$
 (26)

The values of the V_{dg} and V_{qg} are computed by a PI controller and according to the following equations.

$$V'_{dg} = \frac{di_{dg}}{dt} = K_{p2} \left(i_{dg}^* - i_{dg} \right) + K_{I2} \int \left(i_{dg}^* - i_{dg} \right) dt$$

$$V'_{qr} = \frac{di_{qq}}{dt} = K_{p2} \left(i_{qq}^* - i_{qq} \right) + K_{I2} \int \left(i_{qq}^* - i_{qq} \right) dt$$

The elevation angle control system is responsible for increasing or decreasing the elevation angle. By changing the angle of the angular generator speed and as a result, the active power can be kept within the allowed power limit. This controller has feedback on the angular speed of the generator. The reference speed is also set on the maximum speed, which is usually 20% higher than the nominal speed. The resulting error after passing through the PI controller, the reference angle of the reference, results in the reference angle being entered into the distribution system.

When modeling WECSs, sensor dynamics are typically overlooked due to their rapid response compared to the wind turbine dynamics. The anemometer stands out as it is modeled as a first-order low-pass filter with a time constant of 0.5 s.



Sampling is done at a rate of 100 Hz. The recorded signals are subject to Gaussian noise with zero mean and standard deviation as outlined in the Table 2 [42].

TABLE 2. Sensors in WECS.

Standard deviation	The variable to be measured
$0.0158 \mathrm{rad/s}$	Angular speed of the generator
$+0.2^{\circ}$	Pitch angle
$0.025~\mathrm{rad/s}$	Angular speed of the turbine rotor
0.01 m/s^2	Acceleration of the tower
$0.5 \mathrm{m/s}$	Wind speed
0.01 v	Generator voltages
0.01 A	Generator currents

III. TYPE-3 FUZZY LOGIC

T3-FLSs uses developed fuzzy sets that have more degree of freedom in comparison to type-2 counterparts. The secondary memberships in T3-FLSs are fuzzy numbers while in type-2 counterparts are crisp number. This flexibility helps T3-FLSs to represent higher-order uncertainties, allowing for a more detailed modeling of complex systems where uncertainty is not just about membership grades but also about the uncertainty in those grades. This capability makes T3-FLS suitable for applications where uncertainty is multi-dimensional or varies significantly. T3-FLS can adapt more effectively to changes in the environment due to its sophisticated handling of uncertainty, making it suitable for real-time applications. The structure of the T3-FLSs is shown as Fig. 2.

The inputs are generated using $u_i(k)$, $i=1,\ldots,n$ and output y(k). The inputs are denoted by χ_i . The membership functions (MFs) are shown by \tilde{A}_i^j , j-th MF for χ_i . The memberships are written as (see Fig. 3):

$$\begin{split} \bar{\vartheta}_{\tilde{A}_{i}^{j}|\tilde{\rho}_{i}} &= \begin{cases} 1 - \left(\frac{|\chi_{i} - M_{\tilde{A}_{i}^{j}}|}{\underline{Y_{\tilde{A}_{i}^{j}}}}\right)^{\bar{\rho}_{i}} & \text{if } M_{\tilde{A}_{i}^{j}} - \underline{Y_{\tilde{A}_{i}^{j}}} < \chi_{i} \leq M_{\tilde{A}_{i}^{j}} \\ 1 - \left(\frac{|\chi_{i} - M_{\tilde{A}_{i}^{j}}|}{\bar{\gamma}_{\tilde{A}_{i}^{j}}}\right)^{\bar{\rho}_{i}} & \text{if } M_{\tilde{A}_{i}^{j}} < \chi_{i} \leq M_{\tilde{A}_{i}^{j}} + \bar{\gamma}_{\tilde{A}_{i}^{j}} \\ 0 & \text{if } \chi_{i} > M_{\tilde{A}_{i}^{j}} + \bar{\gamma}_{\tilde{A}_{i}^{j}} & \text{or } \chi_{i} < M_{\tilde{A}_{i}^{j}} - \underline{Y_{\tilde{A}_{i}^{j}}} - \underline{Y_{\tilde{A}_{i}^{j}}} \\ 1 - \left(\frac{|\chi_{i} - M_{\tilde{A}_{i}^{j}}|}{\underline{Y_{\tilde{A}_{i}^{j}}}}\right)^{\underline{\rho}_{i}} & \text{if } M_{\tilde{A}_{i}^{j}} - \underline{Y_{\tilde{A}_{i}^{j}}} < \chi_{i} \leq M_{\tilde{A}_{i}^{j}} + \bar{\gamma}_{\tilde{A}_{i}^{j}} \\ 1 - \left(\frac{|\chi_{i} - M_{\tilde{A}_{i}^{j}}|}{\bar{\gamma}_{\tilde{A}_{i}^{j}}}\right)^{\underline{\rho}_{i}} & \text{if } M_{\tilde{A}_{i}^{j}} < \chi_{i} \leq M_{\tilde{A}_{i}^{j}} + \bar{\gamma}_{\tilde{A}_{i}^{j}} \\ 0 & \text{if } \chi_{i} > M_{\tilde{A}_{i}^{j}} + \bar{\gamma}_{\tilde{A}_{i}^{j}} & \text{or } \chi_{i} < M_{\tilde{A}_{i}^{j}} - \underline{Y_{\tilde{A}_{i}^{j}}} < \chi_{i} \leq M_{\tilde{A}_{i}^{j}} \\ 1 - \left(\frac{|\chi_{i} - M_{\tilde{A}_{i}^{j}}|}{\underline{Y_{\tilde{A}_{i}^{j}}}}\right)^{\frac{1}{\underline{\rho}_{i}}} & \text{if } M_{\tilde{A}_{i}^{j}} - \underline{Y_{\tilde{A}_{i}^{j}}} < \chi_{i} \leq M_{\tilde{A}_{i}^{j}} + \bar{\gamma}_{\tilde{A}_{i}^{j}} \\ 1 - \left(\frac{|\chi_{i} - M_{\tilde{A}_{i}^{j}}|}{\underline{Y_{\tilde{A}_{i}^{j}}}}\right)^{\frac{1}{\underline{\rho}_{i}}} & \text{if } M_{\tilde{A}_{i}^{j}} < \chi_{i} \leq M_{\tilde{A}_{i}^{j}} + \bar{\gamma}_{\tilde{A}_{i}^{j}} \\ 0 & \text{if } \chi_{i} > M_{\tilde{A}_{i}^{j}} + \bar{\gamma}_{\tilde{A}_{i}^{j}} & \text{or } \chi_{i} < M_{\tilde{A}_{i}^{j}} + \bar{\gamma}_{\tilde{A}_{i}^{j}} \\ 0 & \text{if } \chi_{i} > M_{\tilde{A}_{i}^{j}} + \bar{\gamma}_{\tilde{A}_{i}^{j}} & \text{or } \chi_{i} < M_{\tilde{A}_{i}^{j}} + \bar{\gamma}_{\tilde{A}_{i}^{j}} \end{cases} \end{cases}$$

$$\underline{\vartheta}_{\tilde{A}_{i}^{j}|\underline{\rho}_{i}} = \begin{cases} 1 - \left(\frac{|\chi_{i} - M_{\tilde{A}_{i}^{j}}|}{\underline{\gamma}_{\tilde{A}_{i}^{j}}}\right)^{\frac{1}{\underline{\rho}_{i}}} \text{if } M_{\tilde{A}_{i}^{j}} - \underline{\gamma}_{\tilde{A}_{i}^{j}} < \chi_{i} \leq M_{\tilde{A}_{i}^{j}} \\ 1 - \left(\frac{|\chi_{i} - M_{\tilde{A}_{i}^{j}}|}{\bar{\gamma}_{\tilde{A}_{i}^{j}}}\right)^{\frac{1}{\underline{\rho}_{i}}} \text{if } M_{\tilde{A}_{i}^{j}} < \chi_{i} \leq M_{\tilde{A}_{i}^{j}} + \bar{\gamma}_{\tilde{A}_{i}^{j}} \\ 0 \qquad \text{if } \chi_{i} > M_{\tilde{A}_{i}^{j}} + \bar{\gamma}_{\tilde{A}_{i}^{j}} \text{ or } \chi_{i} < M_{\tilde{A}_{i}^{j}} - \underline{\gamma}_{\tilde{A}_{i}^{j}} \end{cases}$$

where $\bar{\vartheta}_{\tilde{A}^j_i|\bar{\rho}_i}$, $\bar{\vartheta}_{\tilde{A}^j_i|\bar{\rho}_i}$, $\underline{\vartheta}_{\tilde{A}^j_i|\bar{\rho}_i}$ and $\underline{\vartheta}_{\tilde{A}^j_i|\bar{\rho}_i}$ respectively denote the upper memberships for \tilde{A}^j_i at $\bar{\rho}_i$ and $\underline{\rho}_i$ and the lower memberships for \tilde{A}^j_i at $\bar{\rho}_i$ and $\underline{\rho}_i$, which are not specific values but in the specific interval. $M_{\tilde{A}^j_i}$ expresses the center of \tilde{A}^j_i . Also, $\bar{\gamma}_{\tilde{A}^j_i}$ and $\underline{\gamma}_{\tilde{A}^j_i}$ are the distance of $M_{\tilde{A}^j_i}$ to the start and end points of \tilde{A}^j_i , respectively (see Fig. 3).

The rule firings are given as

$$\begin{split} \bar{\Omega}_{\bar{\rho}_{i}}^{k} &= \Pi_{j=1}^{n} \bar{\vartheta}_{A_{i|\bar{\rho}_{i}}^{p_{j}}} \\ \bar{\Omega}_{\underline{\rho}_{i}}^{k} &= \Pi_{j=1}^{n} \bar{\vartheta}_{A_{i|\bar{\rho}_{i}}^{p_{j}}} \\ \underline{\Omega}_{\bar{\rho}_{i}}^{k} &= \Pi_{j=1}^{n} \underline{\vartheta}_{A_{i|\bar{\rho}_{i}}^{p_{j}}} \\ \underline{\Omega}_{\bar{\rho}_{i}}^{k} &= \Pi_{j=1}^{n} \underline{\vartheta}_{A_{i|\bar{\rho}_{i}}^{p_{j}}} \end{split}$$

The output is:

$$\varpi = \frac{\sum_{i=1}^{n_{\rho}} \left(\underline{\rho}_{i} \underline{\varpi}_{i} + \overline{\rho}_{i} \overline{\varpi}_{i} \right)}{\sum_{i=1}^{n_{\rho}} \left(\underline{\rho}_{i} + \overline{\rho}_{i} \right)}$$

where,

$$\begin{split} \overline{\varpi}_{i} &= \frac{\sum_{k=1}^{n_{r}} \left(\overline{\Omega}_{\overline{\rho}_{i}}^{k} \overline{\eta}_{k} + \underline{\Omega}_{\overline{\rho}_{i}}^{k} \underline{\eta}_{k} \right)}{\sum_{k=1}^{n_{r}} \left(\overline{\Omega}_{\overline{\rho}_{i}}^{k} + \underline{\Omega}_{\overline{\rho}_{i}}^{k} \right)} \\ \underline{\varpi}_{i} &= \frac{\sum_{k=1}^{n_{r}} \left(\overline{\Omega}_{\underline{\rho}_{i}}^{k} \overline{\eta}_{k} + \underline{\Omega}_{\underline{\rho}_{i}}^{k} \underline{\eta}_{k} \right)}{\sum_{k=1}^{n_{r}} \left(\overline{\Omega}_{\rho_{i}}^{k} + \underline{\Omega}_{\rho_{i}}^{k} \right)} \end{split}$$

The output is rewritten as

$$\hat{f}(\chi|\eta) = \eta^{\mathrm{T}}\lambda$$

where

$$\begin{split} \lambda^{\mathrm{T}} &= [\underline{\lambda}_{1}, \cdots, \underline{\lambda}_{n_{r}}, \overline{\lambda}_{1}, \cdots, \overline{\lambda}_{n_{r}}] \\ \eta^{\mathrm{T}} &= [\underline{\eta}_{1}, \cdots, \underline{\eta}_{n_{r}}, \overline{\eta}_{1}, \cdots, \overline{\eta}_{n_{r}}] \\ \underline{\lambda}_{k} &= \frac{\sum_{i=1}^{n_{\rho}} \underline{\rho}_{i} \underline{\Omega}_{\underline{\rho}_{i}}^{k}}{\sum_{i=1}^{n_{\rho}} \left(\underline{\rho}_{i} + \overline{\rho}_{i}\right) \sum_{k=1}^{n_{\rho}} \left(\overline{\Omega}_{\underline{\rho}_{i}}^{k} + \underline{\Omega}_{\underline{\rho}_{i}}^{k}\right)} \\ &+ \frac{\sum_{i=1}^{n_{\rho}} \overline{\rho}_{i} \underline{\Omega}_{\overline{\rho}_{i}}^{k}}{\sum_{i=1}^{n_{\rho}} \left(\underline{\rho}_{i} + \overline{\rho}_{i}\right) \sum_{k=1}^{n_{r}} \left(\overline{\Omega}_{\overline{\rho}_{i}}^{k} + \underline{\Omega}_{\overline{\rho}_{i}}^{k}\right)} \\ \overline{\lambda}_{k} &= \frac{\sum_{i=1}^{n_{\rho}} \underline{\rho}_{i} \overline{\Omega}_{\underline{\rho}_{i}}^{k}}{\sum_{i=1}^{n_{\rho}} \left(\underline{\rho}_{i} + \overline{\rho}_{i}\right) \sum_{k=1}^{n_{r}} \left(\overline{\Omega}_{\underline{\rho}_{i}}^{k} + \underline{\Omega}_{\underline{\rho}_{i}}^{k}\right)} \end{split}$$



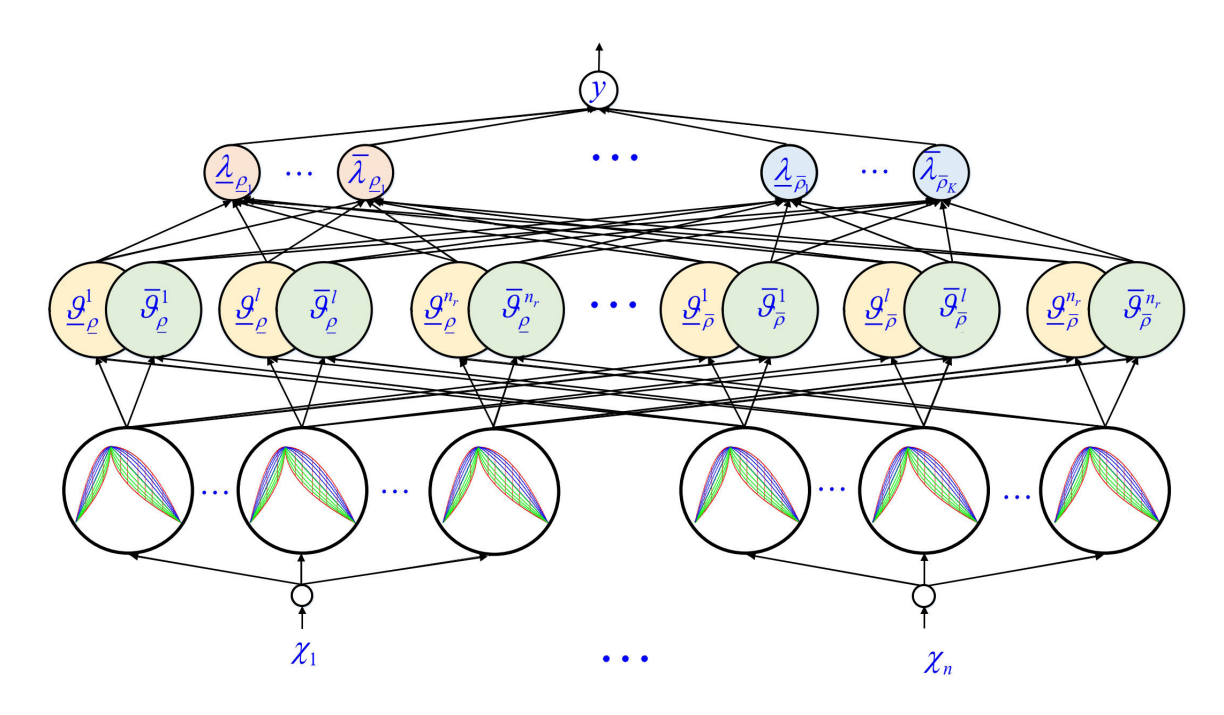


FIGURE 2. The structure of the type-3 FLS.

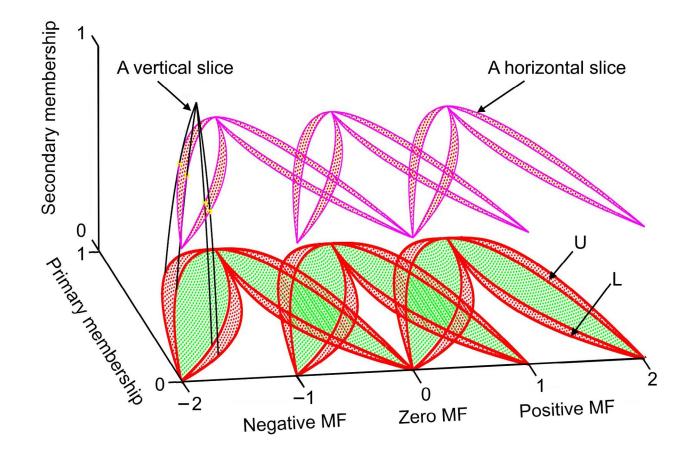


FIGURE 3. Type-3 membership function (MF). The letters "U" and "L" mean the upper and lower bounds of footprint of uncertainty, respectively.

$$+\frac{\sum_{i=1}^{n_{\rho}}\overline{\rho}_{i}\overline{\Omega}_{\overline{\rho}_{i}}^{k}}{\sum_{i=1}^{n_{\rho}}\left(\underline{\rho}_{i}+\overline{\rho}_{i}\right)\sum_{k=1}^{n_{r}}\left(\overline{\Omega}_{\overline{\rho}_{i}}^{k}+\underline{\Omega}_{\overline{\rho}_{i}}^{k}\right)}$$

IV. ADAPTIVE RANDOM SEARCH (ARS) TRAINING

In this research, ARS is employed for T3-FLS training. The advantage of this method is that it can be implemented easily and has a very wide application area. The information required for the implementation of this approach is only the input/output information. The input is the parameter vector θ , while the output is the cost function $J(\theta)$. The parameters of T3-FLS are represented by the vector θ . During training, the objective is to adjust the elements of the vector θ to minimize

the following cost function.

$$\theta^* = \min_{\theta \in \mathbb{C}} J(\theta)$$

where in the relation above θ^* is the vector of optimal parameters of T3-FLS, J represents the cost function, p denotes the dimension of the θ . $J(l;\theta)$ is defined as

$$J(l;\theta) = \frac{1}{2} \sum_{k=1}^{N} (y_{\gamma}(k) - y(k;\theta))^2$$

In the context of ARS, the desired output of T3-FLS, denoted by $y_{\gamma}(k)$, the actual response of T3-FLS to input pattern N, denoted by $y(k;\theta)$, represent the target and practical outcomes, respectively. u(k) signifies the training size, and l is the repetition data index. The cost function should be constructed to minimize the input/output patterns provided. Notably, in ARS, there is no necessity to compute the gradient J. Table 3 shows the stages of the ARS learning algorithm. Considering the sequence $\hat{\theta}_0, \hat{\theta}_1, \ldots, \hat{\theta}_k$ as the answer obtained at time k, to reach the next point, $\hat{\theta}_{k+1}$, the following equation is utilized.

$$\hat{\theta}_{k+1} = \hat{\theta}_k + r_k$$

In the given scenario, $\hat{\theta}_k$ represents the estimated value of θ^* in the k-th iteration, and r_k denotes the randomly generated disturbance vector following a normal distribution $\mathcal{N}(0, \nu)$. The updated estimate $\hat{\theta}_{k+1}$ is determined by comparing the cost functions $J(\hat{\theta}_k)$ and $J(\hat{\theta}_{k+1})$, with leading to a smaller cost function. Otherwise, $\hat{\theta}_{k+1}$ remains unchanged as $\hat{\theta}_k$. To initiate the optimization process, specifying the initial $\hat{\theta}_k$ and the variance of ν is essential. In the pursuit of locating the global minimum θ^* , a large variance for r_k is necessary when



TABLE 3. ARS training algorithm.

```
Step 1: Initial points for \hat{\theta}_0, n_{\text{max}}, J_{\text{min}} and v_0 are selected, and \hat{\theta}_{\text{best}} = \hat{\theta}_0 and
n=1 are placed.
Step 2: The variance selection step. First, k = 1, i = 1 and \hat{\theta}_k = \hat{\theta}_0
are placed, and then the following algorithm is implemented:
While (i < 5)
While (t \le 50/i)
Execution of the algorithm to find the experimental point
t = t + 1; 
i = i + 1;
t = 1;
\hat{\theta}_k = \hat{\theta}_0; }
Step 3: The variance exploitation stage has been selected. In this step,
k = 1, \theta_k = \theta_{\text{best}} and i = i_{\text{best}} are placed and then:
While (t \le 100)
Execution of the algorithm to find the test point
If (n = n_{\text{max}}) or J(\hat{\theta}_{\text{best}}) < J_{\text{min}} then BREAK;
else \hat{\theta}_0 = \hat{\theta}_{\text{best}}, n = n + 1, and go to Step 1;
Algorithm to find the test point:
First, to get \hat{\theta}_k, \hat{\theta}'_k is perturbed with the help of the following equations.
v_i = 10^{-i}v_0 and \hat{\theta}_k' = r_k + \hat{\theta}_k; then the following conditions are checked:
If J(\hat{\theta}'_k) \leq J(\hat{\theta}_k) then \hat{\theta}_{k+1} = \hat{\theta}'_k else \hat{\theta}'_k = \hat{\theta}_k;
If J(\hat{\theta}'_k) \leq J(\hat{\theta}_{\text{best}}) then \hat{\theta}_{\text{best}} = \hat{\theta}'_k else i_{\text{best}} = i.
```

 $\hat{\theta}_k$ is distant from θ^* to cover extensive parameter spaces and prevent getting trapped in local minima. Conversely, a small variance for r_k is preferred when $\hat{\theta}_k$ is close to θ^* . The ARS training process is streamlined with the algorithm's inherent feature of global convergence.

V. PROPOSED FDIS DESIGN PROCESS

In general, possible errors in the WECS can be classified into two categories: mechanical and electrical. In this research, the errors related to the pitch sensor, the pitch engine, and the generator angular speed sensor are examined, because these categories of errors are more severe and important than others have mechanical errors. The internal errors related to the generator and converters were also not considered due to the complexity and widening of the research. The other faults, such as a 3-phase short circuit to the ground fault in the generator bus, and the protection systems that come into action and disconnect the wind turbine from the network, were not taken into consideration. Also, it is assumed that the controllers used in the energy conversion system do not suffer errors and continue to function properly. The operating conditions when the error occurs are as follows.

 The control system does not have any errors and continues to function normally when an error occurs.

- One of the errors related to the pitch sensor, pitch engine, and generator sensor happens asynchronously.
- Other than the mentioned cases, no other error occurs in WECS.

In the fault detection system, checking the two output signals from the speed sensors of the generator angles and pitch angles will identify the error in the generator sensor, and the pitch actuators. According to the modeling done for the wind turbine, both the signals above are considered as a nonlinear function of the rotor angular speed, ω_r , and the wind speed. Because the control performance changes under various speeds. Then,

$$\omega_g = h_1(V_\omega, \omega_r)$$
$$\beta_{1,2,3} = h_2(V_\omega, \omega_r)$$

where $h_1(\cdot)$ and $h_2(\cdot)$ are non-linear functions. Considering the values measured as inputs, their output can be estimated by the mentioned T3-FLS. To train the T3-FLS model of the output of the generator angular speed sensor, training data with the number of 1000 samples in each category were used according to the presented WECS. To test the designed T3-FLS model, the test data set was used, which has 200 samples for an average speed of 16 m/s. The best structures were selected according to the Akaike criteria (AIC) and the final



forecasting error. AIC considers the complexity of the model by minimizing the f_{AIC} . The function f_{AIC} is defined as

$$f_{AIC} = \log(J) + 2K/N$$
,

where N and K are the sample numbers used for training and rule parameter numbers, respectively, and J is the mean squared error between y_i^{γ} and the T3-FLS output y_i . Another well-known criterion is also used in this field, which is the criterion of final prediction error (FPE). The FPE selects the order of the model by minimizing the following function.

$$f_{\text{FPE}} = J(1 + K/N)/(1 - K/N).$$

Remark 1: The proposed parallel operation of T3-FLS models (one simulating normal conditions and the other faulty) facilitates precise error identification, making it a robust solution for real-time diagnostics. Furthermore, the elimination of gradient calculations through ARS simplifies the training process, which is particularly advantageous in dynamic environments. The successful simulation results, showcasing rapid fault detection with minimal false alarms, underscore the approach's practicality and potential for widespread application across various system components.

Remark 2: The threshold can be increased to prevent false alarms caused by noise and interference to reduce misdiagnosis. However, increasing the threshold limit will result in a decrease in the sensitivity of the detection scheme. A trade-off should always be considered between the error diagnosis rate and the sensitivity of FDIS to all types of errors in the design, to minimize the number of incorrect diagnoses and maximize sensitivity. To deal with this issue, in this paper the accuracy of identification of the normal conditions is improved using T3-FLSs and developed global learning algorithm. However, it can be further studied in future studies.

Remark 3: The ARS fine-tunes the parameters of the T3-FLS, which are critical for accurately modeling the behavior of the wind energy conversion system (WECS). By global exploring the parameter space, ARS identifies the optimal settings that improve the system's responsiveness to faults. Also, The ARS helps in determining the appropriate number of rules for the T3-FLS. The ARS does not require gradient calculations, simplifying the optimization process.

VI. SIMULATION

The simulation conditions are described in Table 4. The results related to choosing the appropriate T3-FLS structure for ω_g modeling are shown in Table 5. From Table 5, T3-FLS with least number of rules provide the best results. Finally, according to the results of training and testing, the optimal structure is considered the best model for modeling the behavior of ω_g under normal operating conditions. Figure 4 depicts the comparison of ω_g obtained from the model and ω_g estimated by the dynamic T3-FLS. The designed FLS optimally approximates ω_g .

To form a fault diagnosis and isolation scheme for the angular speed sensor of the generator, several different types of faults were considered and for each of these faults, a fault

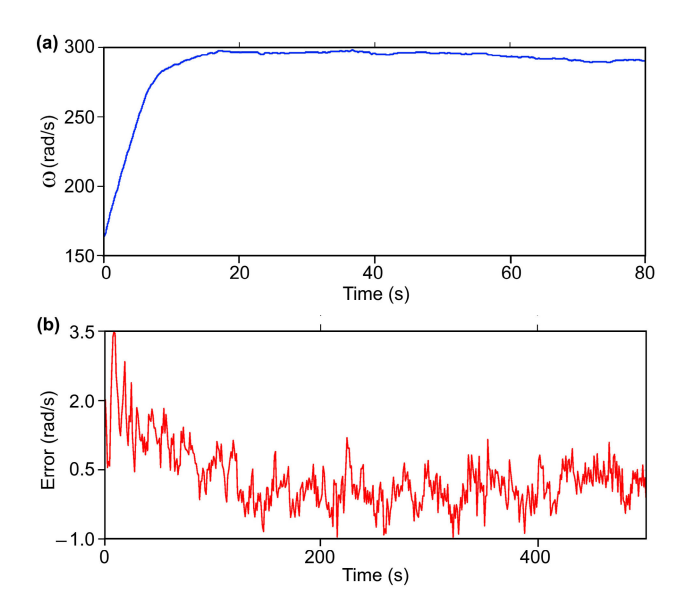


FIGURE 4. (a) Estimated ω_g and (b) Estimation error or residuals. The results are for an average wind speed of 14 m/s and under normal conditions

model was designed by T3-FLS to create a bank of different models for operation modes. The errors considered for the generator angular speed sensor are as follows.

$$f_1^1 = +10\%, f_2^1 = -10\%, f_3^1 = +5\%$$

 $f_4^1 = -5\%, f_5^1 = +2\%, f_6^1 = -2\%.$

Therefore, it is necessary to design a T3-FLS for each type of error and place it in the bank of error models. The design process is the same as the T3-FLS design to estimate the output of the angular velocity sensor. After examining the different structures and according to the mentioned criteria, for errors f_1^1 , f_2^1 , f_3^1 , f_4^1 , f_5^1 and f_6^1 the optimal T3-FLS is selected. As a result, six error states were considered for the angular speed sensor of the generator. From these faulty states, it is possible to find out the amount of error continuously occurring in the generator sensor, in such a way, whether the error happened to a low ($\pm 2\%$), medium ($\pm 5\%$) or high $(\pm 10\%)$ rate. Also, according to the evaluation of the residuals, a simple threshold limit was used, which was considered to be ± 4 rad/s. The selection of this threshold level is done to obtain the desired sensitivity and prevent the occurrence of false alarms. During the first simulation, in the 30th second, a sudden proportional error of +2% was applied to the generator sensor for 20 s, and in the 70th second, a proportional error of -5% was applied to the generator sensor for 20 s.

Figure 5 shows the result of simulation. From Fig. 5, in the scenario of deviation of the angular velocity of the generator from the actual value, a residual is achieved by the error detection system, and by comparing this residual with the threshold level, it is possible to realize the existence of an error in the system. In this form, between 30-40 s and 70-80 s, the obtained balance exceeded the limit of ± 4 rad/s



	_	-		
TARIF 4	The	cimu	lation	conditions

Base	Values	Wind Tu	rbine Data	DFIG Data	
Parameter	Value	Parameter	Value	Parameter	Value
\overline{P}	$2 \mathrm{MW}$	Number of blades	3	Number of poles	4
V_n	$690 \mathrm{\ v}$	N_g	86	L_m	3.29
f_n	$60~\mathrm{Hz}$	ω_n	$8.88~\mathrm{Hz}$	R_s	$0.0069315 \; \mathrm{p.u.}$
$\omega_{ m gnom}$	$195.8 \mathrm{\ rad}/s$	$K_{ m dt}$	1.0384×108	R_r	$0.00906 \; \mathrm{p.u.}$
		$B_{ m dt}$	1.0384×106	$L_{ m ls}$	$0.08084 \mathrm{\ p.u.}$
		h	$60 \mathrm{m}$	$L_{ m lr}$	$0.09934 \mathrm{\ p.u.}$
		R	$31.56 \mathrm{\ m}$	$V_{ m dc,nom}$	1200 v
		J_r	$8.8 \times 106 \; \mathrm{kgm}^2$	C	$10000 \times 10^{-6} F$
		J_g	$150~\mathrm{kgm}^2$	R_g	$0.0015 \; \mathrm{p.u.}$
		$\dot{M_t}$	$251 \times 103 \ \mathrm{kg}$	L_g^-	$0.15 \; \mathrm{p.u.}$
		K_t	$5.56\times106\;\mathrm{Nm}$	-	
		B_t	$2.88 \times 103 \; \mathrm{N/m/s}$		
		$v_{\omega, \; { m cut-in}}$	$4 \mathrm{m/s}$		
		ζ	0.9		
		$v_{\omega, \; ext{cut-off}}$	$25 \mathrm{\ m/s}$		
		ho	$1.225~\mathrm{kg}/m^3$		

and this indicates the occurrence of an error in the generator sensor. The type of error is also found by examining the residuals obtained from faulty neural models; In this way, if the remainder was close to zero, it would indicate the occurrence of that type of error.

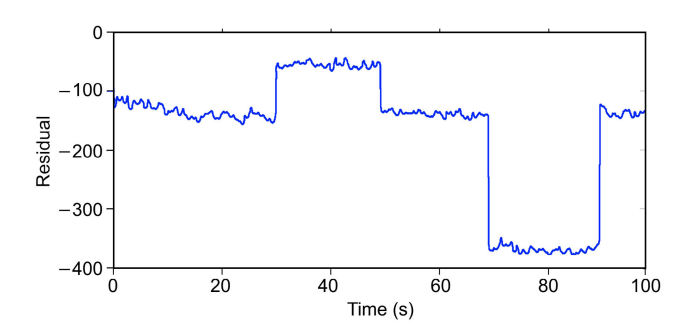


FIGURE 5. The residual of the angular speed of the generator. The results are for an average wind speed of 14 m/s and when a sudden proportional error occurs in the angular speed sensor.

In Fig. 5, only the balance of f_5^1 is close to zero in the period of 30 to 50 s, so an error of +2% has occurred in this period. Also, only the balance of f_4^1 in the time interval from 70 s to 90 s is close to zero, which indicates that -5% error occurred in this interval. In Fig. 5, the residuals from other faulty models have also shown that, as is clear, these residuals have never been in a range close to zero.

The second simulation is related to the occurrence of a soft proportional error in the angular speed. The output of sensor deviates from its original value in the 30th second until it reaches a value of 1.1 equal to its real value in the 90th second; That is, during 60 s, an error equal to +10% of the actual value is created in the angular speed. The result of the simulation in this case is shown in Fig. 6(a). According to Fig. 6(a), the

error detection system can detect the soft error in 40.7 s; That is, a time of about 10.7 s is needed to detect this type of error, which is a good thing for detecting a soft error in the angular speed sensor of the generator.

Finally, the third simulation is related to checking the occurrence of constant output error for the angular speed sensor. In this case, in the 30th second, the output of the angular velocity is kept constant. The remaining signal in this case is given in Fig. 6(b). With the remaining review, it is clear that the error detection system from 34.7 s onwards; That is, only 4.7 s after the occurrence of the error, it can detect it. According to the results obtained for the occurrence of a sudden proportional error, proportional soft error, and fixed output for the angular speed, it can be concluded that the designed error detection system in various speeds. It brings the desired results. This FIDS can detect errors early. A remarkable point in the proposed plan is the very small numbers of false alarms, which is desirable and desirable for any fault diagnosis system.

The following phase of the fault detection system design pertains to the pitch system. Within the pitch system, errors may occur in both the pitch sensor of the vanes and the pitch actuators. To train T3-FLS to model the output of pitch sensor, training data with 1000 samples in each category are used. The ARS was also used to train FLS. The optimal structures are selected according to AIC and FPE criteria. The results related to the selection of the appropriate FLS for the modeling of blade angle are shown in Table 6. According to the results of the table, the T3-FLS with least number of rules with the second order filter was considered for modeling the behavior of β_1 under normal operating conditions. The comparison between the model's β_1 and the dynamic neural network's estimated β_1 and the error in estimation under normal conditions are displayed in Fig. 7.



TABLE 5. Results of dynamic T3-FLS training for training and test data to model ω_q .

		Training data			Test data		
Number of rules	K	\overline{J}	$f_{ m FPE}$	$f_{ m AIC}$	 J	$f_{ m FPE}$	$f_{ m AIC}$
3	31	0.0278	0.0286	-3.5573	0.0124	0.0128	-4.2816
4	41	0.0419	0.0454	-3.0954	0.0434	0.0432	-3.1197
5	51	0.0379	0.0429	-3.1735	0.0419	0.0420	-3.1457
6	25	0.0283	0.0297	-3.5149	0.0116	0.0119	-4.3492
7	33	0.0381	0.0406	-3.2069	0.0210	0.0206	-3.8791
8	41	0.0259	0.0287	-3.5555	0.0141	0.0147	-4.1522
9	50	0.1287	0.1422	-1.9511	0.0355	0.0174	-3.2605

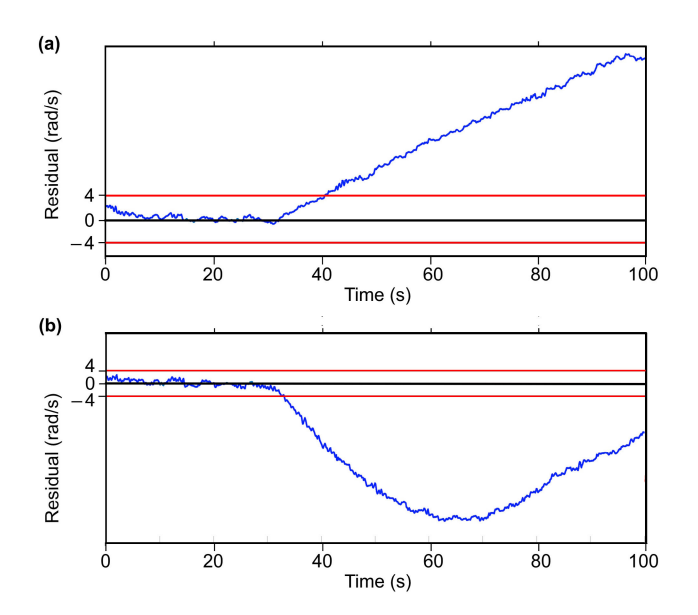
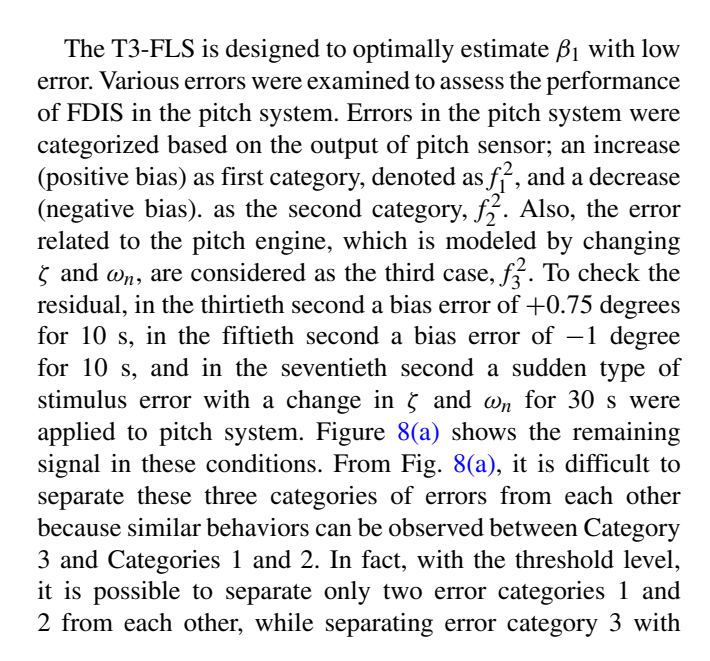


FIGURE 6. The residual signal of the angular velocity of the generator for (a) an average wind speed of 12 m/s and when a soft proportional error occurs in the angular velocity and (b) an average wind speed of 8 m/s and when a constant output error occurs in the sensor of the angular speed of the generator.



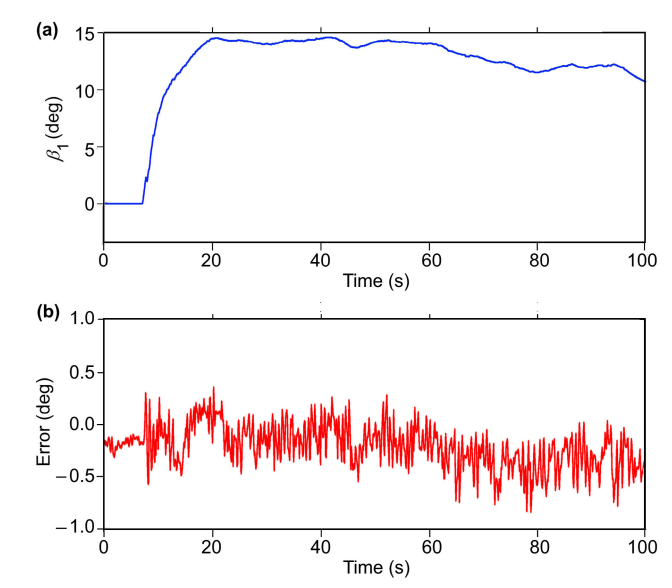


FIGURE 7. Simulation results of WECS for an average wind speed of 14 m/s and under normal conditions: (a) estimated β_1 and (b) residuals (error).

the threshold level would be wrong because this category sometimes has similar behavior to Category 1, and at other times with Category 2, causing a wrong decision. However, it is possible to identify the error that occurred in the pitch system by evaluating the obtained balance and the threshold level. For this purpose, a threshold level of ± 0.3 degrees has been considered for the evaluation of the balance, and the results show that the detection of errors is done well in any case. According to Fig. 8, the positive bias error is 1.3 s, the negative bias error is 2.1 s, and the trigger error is more than 2.5 s after its occurrence.

By using this FDIS, identifying the positive/negative bias errors of the sensor up to ± 0.5 degrees is possible. To speed up the diagnosis time, the value of the threshold can be reduced, but the decreasing of the diagnosis time will coincide with the occurrence of wrong diagnoses.

The suggestion that is made to isolate the error is to use the average of the balance in short periods. According to Fig. 8, it can be noted that the average of the remaining signal increases during the period of the occurrence of an error with



		Educational data				Test data		
Number of rules	K	\overline{J}	f_{FPE}	f_{AIC}	\overline{J}	f_{FPE}	$f_{ m AIC}$	
3	31	0.0404	0.0335	-3.4262	0.0794	0.0714	-2.5035	
4	41	0.0881	0.0864	-2.4610	0.1088	0.1024	-2.1866	
5	51	0.0571	0.0536	-2.9451	0.1047	0.1082	-2.2143	
6	25	0.2547	0.2593	-1.3537	0.2520	0.2473	-1.3563	
7	33	0.1123	0.1199	-2.2084	0.1481	0.1521	-1.8846	
8	41	0.0494	0.0441	-3.1452	0.0831	0.0895	-2.4598	
9	50	0.0741	0.0724	-2.6391	0.0962	0.0751	-2.3028	

TABLE 6. Results of T3-FLS training for training/test data to model β_1 .

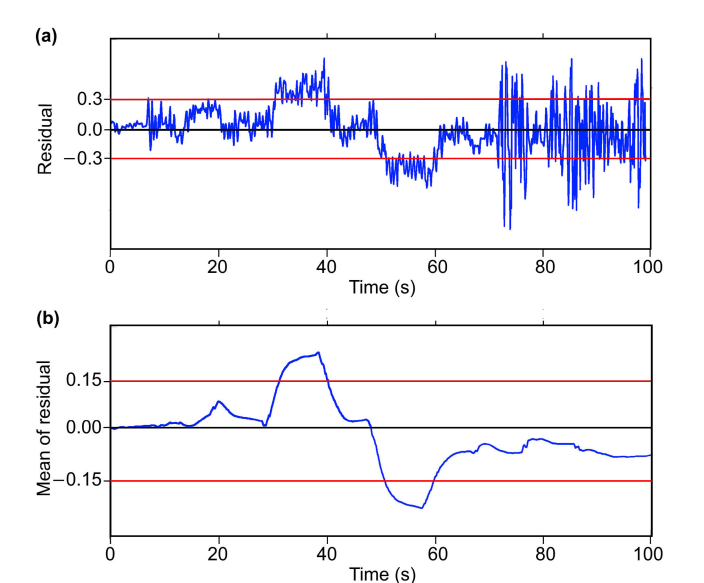


FIGURE 8. (a) Evaluation of the residual by the specified threshold for the average speed of 15 m/s in the conditions of all three types of errors in the pitch subsystem and (b) The average of the residual during the time intervals of 10 s during the happening of all three type of errors in the one pitch system.

positive bias and decreases during the period of the error occurrence with negative bias. Also, in the time interval of the occurrence of the motor error, there is not much change in the remaining Yangin current. To check the correctness of the suggested scheme, the simulations were performed again when three types of errors occurred and the average of the remaining signal was calculated in 10-second intervals. The result of the simulation is illustrated in Fig. 9.

The average of the balance in the period of occurrence of positive bias error (between 30 s and 40 s) has increased and in the period of occurrence of negative bias error (between 50 s and 60 s), it has decreased. In period 70-100 s, it has remained in a range close to zero. Therefore, the operations related to error diagnosis and isolation for the pitch system can be summarized as follows.

• If the balance obtained from the pitch system exceeds the specified threshold, it indicates that a fault has happened in the pitch component. The type of error is also found according to the following process.

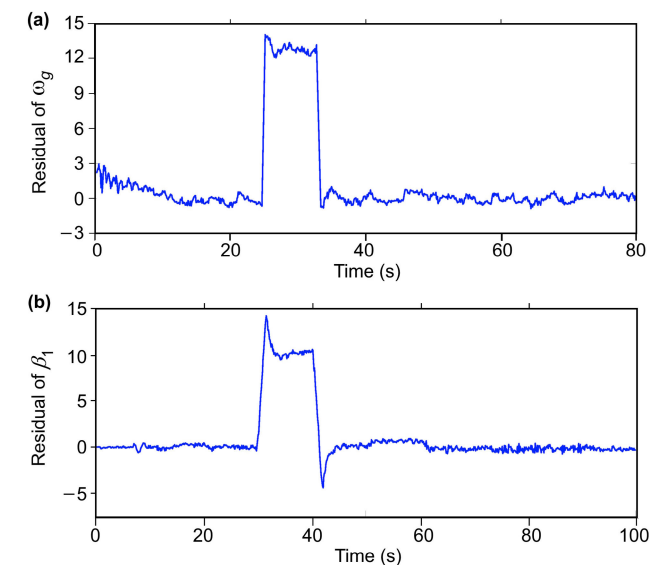


FIGURE 9. Residual signals when three types of errors occur in the angular speed sensor and actuator: (a) the residual for error detection of generator angular speed sensor and (b) the residual for error detection of pitch system.

- 1) If the residual average is more than the upper threshold, category 1 error; meaning that positive bias has occurred.
- 2) If the remaining average is less than the lower threshold, category 2 error; meaning that negative bias has happened.
- 3) If the remaining average does not exceed the specified threshold level, it indicates that an error has happened in the pitch driver.
- If the resulting balance does not exceed the threshold, an error has not occurred in the overflow system.

VII. DISCUSSION

The pre-operation phase involved separate investigations of the fault detection systems for the generator sensor and pitch system. This section aims to evaluate the overall efficiency of the suggested fault detection under conditions where errors in the angular speed sensor, pitch sensor, and pitch actuator do not occur simultaneously. It is important to note



TABLE 7. Sensors in WECS.

Start time	End time	Error type	Error location
40	80	Proportionality of $+2\%$	Generator sensor
70	130	Decay of hydraulic pump (change ζ and ω_n)	Pitch stimulant
120	150	Proportionality -10%	Generator sensor
150	185	Positive bias $+1^{\circ}$	Pitch sensor
190	210	Proportionality of $+5\%$	Generator sensor
225	235	Proportionality -2%	Generator sensor
245	265	Negative bias -8°	Pitch sensor
265	290	High volume of air in hydraulic oil (change ζ and ω_n)	Pitch stimulant

that an error in the generator's angular speed sensor can impact the accuracy of the generator error detection system. To investigate this matter, the error of the generator sensor in the thirtieth second is +5% for 10 s, the error of the pitch sensor in the fiftieth second is +1 degree for 10 s, and the error of the pitch actuator in the seventieth second, due to the type of hydraulic pump decay, for 20 s, was applied to pitch system.

As it is clear from the results, with the occurrence of an error in the generator sensor, the balance related to the 1st vane system has also been affected and changed. On the contrary, with the occurrence of an error in the sensor or the actuator, there is no change in the rest related to the angular speed of the generator. Therefore, to form a unified FDIS, this point should be considered if both of the resulting balances change and cross the threshold. This indicates that if the balance related to the pitch angle of the blade exceeds the threshold level, it signifies an error in the pitch system. The algorithm described in the previous section can be applied to identify the ongoing error in the pitch system. The steps of the general algorithm for diagnosing and isolating the investigated errors are as

- 1) If the differences between the angular speed sensor residuals and the 1st blade system residuals are both below the threshold, then there is no error in the system.
- 2) If the residuals from the speed sensor and the pitch system are both out of the threshold, an error has happened in the sensor. The type of error is also obtained according to the faulty FLS models and the comparison of their residuals with the threshold.
- 3) If the residual of the angular speed sensor is within the specified threshold, but the residual of the pitch system is out of the specified threshold, an error has been happened in the pitch subsystem. The type of error is determined according to the suggestion presented in the previous section. If the remaining average is higher than the threshold, it is a positive bias error, if it is less than the lower threshold, it is a negative bias error, and if it is within the threshold level, it is a rising error.

To check the accuracy of the FDIS operation along with the presented algorithm, according to Table 7, different errors are shown in time intervals and applied to the system over 300 s. As it is clear from the results of the simulation, FDIS has a very favorable performance with the least error in diagnosing errors. To decrease the wrong diagnoses numbers, the threshold can be raised to prevent false alarms due to noise, and disturbances. However, increasing the threshold limit will result in a decrease in the sensitivity of the detection scheme. A trade-off should always be considered between the rate of false diagnosis and the sensitivity of FDIS to all types of errors in the design so that the false diagnosis number is low and the sensitivity is as high as possible. The algorithm exhibited strong performance, demonstrating minimal error rates in diagnosing faults. Future work will explore adaptive thresholding techniques and a broader range of performance metrics to optimize the algorithm's performance in real-world scenarios.

VIII. CONCLUSION

In this research, by using the dynamic model of the wind energy systems that include both mechanical and electrical parts, a fault detection and isolation system is designed. The continuous faults are detected in the angular speed sensor of the generator and pitch's sensors and actuators. Diagnosing and isolating the continuously occurring errors in the wind energy conversion system is done using T3-FLSs. A dynamic T3-FLS imitates the system's normal behavior and another model imitates the faulty conditions. T3-FLS models are placed in parallel with the real plant and their outputs are compared with the real outputs of the system. Thus, the time and location of the error in the real system are identified. The adaptive random search is used to train T3-FLSs, which do not need to calculate gradient expressions. A suitable number of rules for the T3-FLS are also selected based on the AIC and FPE criteria. The simulation results show that FDIS works fast, accurately, and correctly with the presented algorithm. Its false alarm rate is seldom and isolates the identified errors well. The presented method can be used to diagnose the error of other components of the wind energy system, such as the gear wheel.

REFERENCES

[1] M. M. Mahmoud, B. S. Atia, Y. M. Esmail, S. A. E. M. Ardjoun, N. Anwer, A. I. Omar, F. Alsaif, S. Alsulamy, and S. A. Mohamed, "Application of whale optimization algorithm based FOPI controllers for STATCOM and UPQC to mitigate harmonics and voltage instability in modern distribution power grids," *Axioms*, vol. 12, no. 5, p. 420, Apr. 2023.



- [2] X. Hu, T. Tang, L. Tan, and H. Zhang, "Fault detection for point machines: A review, challenges, and perspectives," *Actuators*, vol. 12, no. 10, p. 391, Oct. 2023.
- [3] S. Zhi, H. Shen, and T. Wang, "Gearbox localized fault detection based on meshing frequency modulation analysis," *Appl. Acoust.*, vol. 219, Mar. 2024, Art. no. 109943.
- [4] D. Zhao, H. Wang, and L. Cui, "Frequency-chirprate synchrosqueezing-based scaling chirplet transform for wind turbine nonstationary fault feature time-frequency representation," *Mech. Syst. Signal Process.*, vol. 209, Mar. 2024, Art. no. 111112.
- [5] M. A. D. D. O. Ferreira, L. C. Ribeiro, H. S. Schuffner, M. P. Libório, and P. I. Ekel, "Fuzzy-set-based multi-attribute decision-making, its computing implementation, and applications," *Axioms*, vol. 13, no. 3, p. 142, Feb. 2024.
- [6] A. Karami-Mollaee and O. Barambones, "Pitch control of wind turbine blades using fractional particle swarm optimization," *Axioms*, vol. 12, no. 1, p. 25, Dec. 2022.
- [7] J. Zhang, D. Yang, W. Li, H. Zhang, G. Li, and P. Gu, "Resilient output control of multiagent systems with DoS attacks and actuator faults: Fully distributed event-triggered approach," *IEEE Trans. Cybern.*, early access, Jun. 27, 2024, doi: 10.1109/TCYB.2024.3404010.
- [8] S. R. Kabat, C. K. Panigrahi, and B. P. Ganthia, "Fuzzy logic based fault current prediction in double fed induction generator based wind turbine system," *Mater. Today, Proc.*, vol. 80, pp. 2530–2538, Jan. 2023.
- [9] Z. Wang, G. Li, L. Yao, Y. Cai, T. Lin, J. Zhang, and H. Dong, "Intelligent fault detection scheme for constant-speed wind turbines based on improved multiscale fuzzy entropy and adaptive chaotic Aquila optimization-based support vector machine," ISA Trans., vol. 138, pp. 582–602, Jul. 2023.
- [10] P. W. Khan, C. Y. Yeun, and Y. C. Byun, "Fault detection of wind turbines using SCADA data and genetic algorithm-based ensemble learning," *Eng. Failure Anal.*, vol. 148, Jun. 2023, Art. no. 107209.
- [11] P. Climaco, J. Garcke, and R. Iza-Teran, "Multi-resolution dynamic mode decomposition for damage detection in wind turbine gearboxes," *Data-Centric Eng.*, vol. 4, p. e1, Jan. 2023.
- [12] G. Alipoor, S. J. Mirbagheri, S. M. M. Moosavi, and S. M. A. Cruz, "Incipient detection of stator inter-turn short-circuit faults in a doubly-fed induction generator using deep learning," *IET Electr. Power Appl.*, vol. 17, no. 2, pp. 256–267, Feb. 2023.
- [13] X. Yanbin, Z. Jianhua, X. Wang, M. Shabaz, M. W. Ahmad, and S. Ray, "Research on optimization of crane fault predictive control system based on data mining," *Nonlinear Eng.*, vol. 12, no. 1, Jan. 2023, Art. no. 20220202.
- [14] Y. Cheng, J. Wang, K. Dai, and A. El Damatty, "Influence of mechanical faults in pitch, brake, controller systems on fragility of offshore wind turbine under aero-hydro loadings," *Ocean Eng.*, vol. 285, Oct. 2023, Art. no. 115386.
- [15] J. Liang and K. Zhang, "A new hybrid fault diagnosis method for wind energy converters," *Electronics*, vol. 12, no. 5, p. 1263, Mar. 2023.
- [16] P. Sudhakar, N. K. Kamble, G. K, A. V. Turukmane, S. B. Perli, and P. Jayaraman, "Faulty diagnostics model for wind power plant application using AI," *Meas.*, *Sensors*, vol. 25, Feb. 2023, Art. no. 100621.
- [17] P. Dore, S. Chakkor, A. E. Oualkadi, and M. Baghouri, "Real-time intelligent system for wind turbine monitoring using fuzzy system," e-Prime Adv. Electr. Eng., Electron. Energy, vol. 3, Mar. 2023, Art. no. 100096.
- [18] K. Dhibi, M. Mansouri, M. Hajji, K. Bouzrara, H. Nounou, and M. Nounou, "A novel hybrid methodology for fault diagnosis of wind energy conversion systems," *Energy Rep.*, vol. 9, pp. 5362–5371, Dec. 2023.
- [19] E. Chetouani, Y. Errami, A. Obbadi, and S. Sahnoun, "Self-adapting PI controller for grid-connected DFIG wind turbines based on recurrent neural network optimization control under unbalanced grid faults," *Electr. Power Syst. Res.*, vol. 214, Jan. 2023, Art. no. 108829.
- [20] N. Talebi, M. A. Sadrnia, and A. Darabi, "Robust fault detection of wind energy conversion systems based on dynamic neural networks," *Comput. Intell. Neurosci.*, vol. 2014, pp. 1–13, Jan. 2014, doi: 10.1155/2014/580972.
- [21] B. P. Ganthia and S. K. Barik, "Fault analysis of PI and fuzzy-logic-controlled DFIG-based grid-connected wind energy conversion system," J. Inst. Eng. (India), Ser. B, vol. 103, no. 2, pp. 415–437, Apr. 2022.
- [22] E.-J. Pérez-Pérez, V. Puig, F.-R. López-Estrada, G. Valencia-Palomo, I. Santos-Ruiz, and S. E. Samada, "Fault detection and isolation in wind turbines based on neuro-fuzzy qLPV zonotopic observers," *Mech. Syst. Signal Process.*, vol. 191, May 2023, Art. no. 110183.

- [23] X. Li, L. Xie, B. Deng, H. Lu, Y. Zhu, M. Yin, G. Yin, and W. Gao, "Deep dynamic high-order graph convolutional network for wear fault diagnosis of hydrodynamic mechanical seal," *Rel. Eng. Syst. Saf.*, vol. 247, Jul. 2024, Art. no. 110117.
- [24] L. Wu, H. Huang, M. Wang, K. A. Alattas, A. Mohammadzadeh, and E. Ghaderpour, "Optimal control of non-holonomic robotic systems based on type-3 fuzzy model," *IEEE Access*, vol. 11, pp. 124430–124440, 2023.
- [25] L. Xia, G. Chen, T. Wu, Y. Gao, A. Mohammadzadeh, and E. Ghaderpour, "Optimal intelligent control for doubly fed induction generators," *Mathematics*, vol. 11, no. 1, p. 20, Dec. 2022.
- [26] P. Brusola, S. Garcia-Nieto, J. V. Salcedo, M. Martinez, and R. H. Bishop, "Fuzzy modeling framework using sector non-linearity techniques for fixed-wing aircrafts," *Aerospace*, vol. 11, no. 4, p. 258, Mar. 2024.
- [27] S.-R. Yan, Y. Dai, A. D. Shakibjoo, L. Zhu, S. Taghizadeh, E. Ghaderpour, and A. Mohammadzadeh, "A fractional-order multiple-model type-2 fuzzy control for interconnected power systems incorporating renewable energies and demand response," *Energy Rep.*, vol. 12, pp. 187–196, Dec. 2024.
- [28] P. Anbalagan and Y. H. Joo, "Nonfragile sampled-data control for interval type-2 fuzzy modeling of permanent magnet synchronous generator-based wind turbine systems," *IEEE Trans. Syst. Man, Cybern. Syst.*, vol. 54, no. 4, pp. 2426–2439, Apr. 2024.
- [29] L. Xiang, H. Sang, and F. Qu, "A type 2 fuzzy logic-based maintenance solution for power system in renewable energy applications," *Frontiers Energy Res.*, vol. 9, Dec. 2021, Art. no. 762360.
- [30] M. Deveci, U. Cali, S. Kucuksari, and N. Erdogan, "Interval type-2 fuzzy sets based multi-criteria decision-making model for offshore wind farm development in Ireland," *Energy*, vol. 198, May 2020, Art. no. 117317.
- [31] A. Ebrahimi, A. Hajipour, and R. Roshanfekr, "Stator winding short circuit fault detection in three-phase induction motors using combination type-2 fuzzy logic and support vector machine classifier optimized by fractionalorder chaotic particle swarm optimization algorithm," *Comput. Intell. Elect. Eng.*, vol. 12, no. 1, pp. 37–48, 2021.
- [32] H. R. Patel and V. A. Shah, "Shadowed type-2 fuzzy sets in dynamic parameter adaption in cuckoo search and flower pollination algorithms for optimal design of fuzzy fault-tolerant controllers," *Math. Comput. Appl.*, vol. 27, no. 6, p. 89, Oct. 2022.
- [33] Y. Ren, Y. Wen, F. Liu, and Y. Zhang, "A short-term wind speed prediction method based on interval type 2 fuzzy model considering the selection of important input variables," J. Wind Eng. Ind. Aerodynamics, vol. 225, Jun. 2022, Art. no. 104990.
- [34] D. J. Singh, N. K. Verma, A. K. Ghosh, and A. Malagaudanavar, "An approach towards the design of interval type-3 T–S fuzzy system," *IEEE Trans. Fuzzy Syst.*, vol. 30, no. 9, pp. 3880–3893, Sep. 2022.
- [35] A. Taghieh, C. Zhang, K. A. Alattas, Y. Bouteraa, S. Rathinasamy, and A. Mohammadzadeh, "A predictive type-3 fuzzy control for underactuated surface vehicles," *Ocean Eng.*, vol. 266, Dec. 2022, Art. no. 113014.
- [36] D. J. Singh and N. K. Verma, "Interval type-3 T-S fuzzy system for nonlinear aerodynamic modeling," Appl. Soft Comput., vol. 150, Jan. 2024, Art. no. 111097.
- [37] P. Melin and O. Castillo, "An interval type-3 fuzzy-fractal approach for plant monitoring," *Axioms*, vol. 12, no. 8, p. 741, Jul 2023
- [38] P. Ochoa, O. Castillo, P. Melin, and J. R. Castro, "Interval type-3 fuzzy differential evolution for parameterization of fuzzy controllers," *Int. J. Fuzzy Syst.*, vol. 25, no. 4, pp. 1360–1376, Jun. 2023.
- [39] H. Bie, P. Li, F. Chen, and E. Ghaderpour, "An observer-based type-3 fuzzy control for non-holonomic wheeled robots," *Symmetry*, vol. 15, no. 7, p. 1354, Jul. 2023.
- [40] O. Castillo, J. R. Castro, and P. Melin, "Forecasting the COVID-19 with interval type-3 fuzzy logic and the fractal dimension," *Int. J. Fuzzy Syst.*, vol. 25, no. 1, pp. 182–197, Feb. 2023.
- [41] C. Peraza, O. Castillo, P. Melin, J. R. Castro, J. H. Yoon, and Z. W. Geem, "A type-3 fuzzy parameter adjustment in harmony search for the parameterization of fuzzy controllers," *Int. J. Fuzzy Syst.*, vol. 25, no. 6, pp. 2281–2294, Sep. 2023.
- [42] C. Sloth, T. Esbensen, and J. Stoustrup, "Active and passive fault-tolerant LPV control of wind turbines," in *Proc. Amer. Control Conf.*, Jun. 2010, pp. 4640–4646.
- [43] J. Gertler, "Fault detection and diagnosis," in *Encyclopedia of Systems and Control*. Cham, Switzerland: Springer, 2021, pp. 764–769.
- [44] R. Pena, J. C. Clare, and G. M. Asher, "Doubly fed induction generator using back-to-back PWM converters and its application to variable-speed wind-energy generation," *IEE Proc. Electr. Power Appl.*, vol. 143, no. 3, p. 231, 1996.





AIMEI ZHOU is currently an Associate Professor with the School of Graduation, Anhui University of Science and Technology. He is also with Zhejiang Guangsha Vocational and Technical University of Construction. His research interests include motor and motor control.



HAMID TAGHAVIFAR (Senior Member, IEEE) is currently an Assistant Professor with the Department of Mechanical, Industrial and Aerospace Engineering, Concordia University, Montreal, Canada. He has contributed more than 65 peer reviewed articles, a book, and a book chapter, with several registered patents. His research interests include control theory, automated driving, mechatronics, and robotics. He is an Associate Editor of IEEE Transactions on Vehicular Technology and *Journal of Field Robotics*.



ZHIPING ZHU is currently a Senior Engineer with the School of Graduation, Anhui University of Science and Technology. He is also with Zhejiang LINIX Motor Company Ltd. His research interests include motor and motor control.



EBRAHIM GHADERPOUR received the first Ph.D. degree in theoretical and computational and the second Ph.D. degree in remote sensing from Canada, in 2013 and 2018, respectively. He is currently an Assistant Professor with the Department of Earth Sciences, Sapienza University of Rome, Italy. He is also the CEO of Earth and Space Inc., Calgary, AB, Canada. His research interests include big data analytics and artificial intelligence with their applications in remote sensing, geology,

geosciences, robotics, and medicine. He is an academic editor and a reviewer of many journals and publishers.



ARDASHIR MOHAMMADZADEH is a Professor at Shenyang University of Technology, Shenyang, China. He also collaborates with Astana IT University and University of Bonab. He is an academic editor of applied soft computing, and PLOS one. He has published more than 150 papers, and three books. His research interests include control theory, fuzzy logic systems, machine learning, neural networks, intelligent control, electric vehicles, power systems control,

chaotic systems, and medical systems.



ALI DOKHT SHAKIBJOO received the M.Sc. and Ph.D. degrees in electrical engineering from Shahid Rajaee Teacher Training University (SRU), Tehran, Iran, in 2014 and 2022, respectively. He is currently a Lecturer with the Department of Electrical Engineering, Ahrar Institute of Technology and Higher Education, Rasht, Iran. His current research interests include power systems, renewable energy, energy storage, fuzzy systems, and neural networks.



CHUNWEI ZHANG received the degree from Harbin Institute of Technology, in 2005. He is currently the Chair Distinguished Professor, a Ph.D. Supervisor, and the Discipline Leader with Shenyang University of Technology (SUT), China. His research interests include structural control, structural health monitoring, AI, smart materials, and structures.

• •

Open Access funding provided by 'Università degli Studi di Roma "La Sapienza" 2' within the CRUI CARE Agreement